# Multiple-scattering theoretical approach to magnetic dichroism and spin polarization in angle-resolved core-level photoemission

J. Henk, A. M. N. Niklasson, and B. Johansson
*Condensed Matter Theory Group, Department of Physics, University Uppsala, S-751 21 Uppsala, Sweden*
(Received 20 November 1998)

Magnetic dichroism in spin- and angle-resolved core-level photoemission is investigated within the relativistic one-step model of photoemission based on multiple-scattering theory. Photoelectron scattering in emission from $3p$ levels of low-index Fe and Ni surfaces is found to affect intensities, dichroism, and photoelectron spin polarizations considerably, in particular in off-normal emission. In general, the calculated spectra agree well with their experimental counterparts in spectral shape, size of the dichroic signal, and spin polarization. Magnetic circular dichroism in a chiral setup is analyzed theoretically using appropriately defined asymmetries. Further, core-level energy positions and photoemission are compared with those obtained within an atomic model. [S0163-1829(99)10621-0]

## I. INTRODUCTION

Since the pioneering work by Baumgarten *et al.*,[1] magnetic dichroism (MD) in photoemission, i.e., the change of the photocurrent by reversal of the magnetization direction, from both core levels and valence bands has developed into a powerful tool for the investigation of the electronic and magnetic properties of ferromagnetic systems. The main origin of the effect can be regarded as a reduction of symmetry: (i) Originating from spin-orbit coupling (SOC), the local magnetic moments are coupled to the lattice which leads to a certain direction of the magnetization of the ferromagnet (magnetic anisotropy). (ii) For a given photoemission setup (light polarization and incidence direction, emission direction, and surface symmetry) the symmetry of the total system is reduced with respect to the nonmagnetic case. If the remaining symmetry is small enough, e.g., if there is no symmetry operation which leaves the setup invariant but reverses the magnetization direction, then there is in general magnetic dichroism. These simple symmetry considerations allow us to determine in which setups MD occurs. For the investigation of its microscopic origin, however, more detailed models are necessary.

The theoretical descriptions of MD in core-level photoemission can be cast into four categories. On the one hand, there are one-particle (ground-state) and many-body (excited-state) theories; on the other hand, there are theories for single atoms and those which take into account the solid, in particular photoelectron diffraction. To name a few from each category, for atomic one-particle theories we refer to Refs. 2 and 3, for atomic many-particle (multiplet) theory to Refs. 4–7, for solid many-particle theories to Ref. 8, and for solid one-particle theories to Refs. 9–12 (photoelectron diffraction). A multiple-scattering approach to MD, i.e., a solid-state one-particle theory, has been proposed by Ebert *et al.*[13,14] and Tamura *et al.*[15]

In the case of MD in valence-band photoemission, theoretical descriptions have been given by Venus (see, for example, Refs. 16–18 and references therein) which are based on symmetry considerations and analytical calculations within the one-step model of photoemission. Applying group theory and relativistic one-step photoemission theory, Feder's group has developed a consistent picture of MD by combining symmetry considerations with analytical and numerical calculations for realistic systems (see for an introduction Ref. 19, for details Refs. 20–24), the latter allowing for a direct comparison between experiment and theory.[25–28] The analytical work[22] reveals the microscopic origin of MD and establishes a close connection with spin-polarization effects in photoemission from nonmagnetic solids[29–32] which can be condensed into a ''general rule'' of MD: if in a given setup a component of the photoelectron's spin polarization parallel to the magnetization is produced in the nonmagnetic limit, then there is magnetic dichroism. This rule of thumb allows—by simple symmetry considerations—a quick check of whether in a certain geometry there will be MD or not. Further, because it is not specific to valence-band or core-level photoemission, it is valid in both cases. The above interplay between spin-orbit coupling and exchange splitting allows detailed statements about the electronic states involved in the photoemission process.

Using a chiral setup—light incidence direction, surface normal, and electron detection direction span the whole space—photoemission from ferromagnetic surfaces can lead to so-called ''double'' dichroism, i.e., a combination of circular dichroism in angular distribution which is also present in nonmagnetic systems (see, for example, Refs. 33 and 34) with magnetic dichroism. The first effect can be seen as due to interference of partial waves of the outgoing photoelectron, whereas the latter effect is mainly an initial-state effect.[35] For valence-band photoemission from Ni films on Cu(001) we have shown how to separate both effects.[24] In core-level photoemission such an investigation is still missing. Therefore, we investigate in particular the effect of photoelectron scattering, e.g., the very manifestation of the solid state, on ''double'' dichroism.

In this paper, we apply multiple-scattering theoretical methods—which have been successfully used in order to describe MD in valence-band photoemission—to magnetic dichroism in core-level photoemission with the aim to investigate in detail the effect of scattering of the outgoing

 

photoelectron on MD and its spin polarization. Emission from $2p$ and $3p$ levels of Fe(001) and Fe(110) lends themselves support as prototypical systems because a vast amount of experimental and theoretical data is available for these systems. The $3p$ levels of Fe are of particular interest because for them spin-orbit coupling strength and exchange splitting are approximately of the same magnitude, in contrast to the $2p$ levels for which spin-orbit coupling dominates. Further, we take a look on magnetic linear dichroism from $3p$ levels of Ni(110). Analytical calculations within an atomic context allow for a detailed understanding of MD in core-level photoemission which at a first glance is not provided by multiple-scattering calculations. We therefore propose a simple analytical model of core-level photoemission in order to explain basic properties of the spectra.

In Sec. II we briefly describe the numerical methods and ingredients used in the photoemission calculations. In Sec. III a simple analytical model for magnetic dichroism from atoms is proposed. In Sec. IV we discuss magnetic dichroism from Fe $2p$ and Fe $3p$ levels at (001) surfaces as well as Ni(110) $3p$.

## II. NUMERICAL ASPECTS

The numerical calculations are based on the relativistic one-step model of photoemission[36] as implemented within the spin-polarized relativistic layer Korringa-Kohn-Rostoker (KKR) framework.[37] Self-consistent spin- and layer-dependent muffin-tin potentials were obtained by linear muffin-tin orbital (LMTO) calculations within the local spin-density approximation[38,39] for semi-infinite systems and serve as input for the layer-KKR electron-spectroscopy computer program. These potentials account for the enhanced magnetic moments at the surface as well as surface core-level shifts within the initial-state picture.[40–42]

Instead of using a relativistic extension of a PEOVER-type calculation[43–46]—which our program can also use—we calculate the Green's function of the semi-infinite system directly[47,48] which allows both easy access to and modification of physical properties. In fact, both methods give identical results but Pendry's method is computationally much faster.

To investigate the effect of photoelectron scattering, we performed calculations—besides fully ones—with the single-site scattering matrices of all sites for the photoelectron state set equal to zero. All other parameters remained unchanged. In particular, the wave function of the photoelectron within the muffin-tin spheres was not changed, thus using identical transition-matrix elements in both calculations. And further, exchange splitting and SOC are always taken into account in the photoelectron's wave function. This procedure allows a detailed analysis of how the band structure affects the dichroic photoemission intensities. We would like to note that we are not performing an atomic calculation, because the excitation processes take place at each site and lead to a stationary photoelectron wave function (see, for example, Ref. 49). We denote calculations and their results with photoelectron scattering included as ''pes,'' those without photoelectron scattering as ''nopes.'' If in addition the surface barrier has been switched off, we refer to ''nopesb.''

We would like to stress that our multiple-scattering calculations are fully converged by taking into account the scattering properties of the whole semi-infinite solid. (For a comparison of convergence in multiple-scattering and photoelectron diffraction calculations using clusters see Refs. 50 and 51.) Multiple-scattering calculations on MD have been performed, for example, by Ebert and Guo,[14,52] and photoelectron diffraction has been addressed by Hart and Beeby.[53]

A many-particle calculation is beyond the scope of the present paper because we are interested mainly in effects related to the photoelectron and the latter are usually not included in many-body theories.[8,11] However, many-body effects are taken into account in two ways in KKR-type calculations. Core-hole lifetimes depend in principle on the spin: majority states show smaller lifetimes than minority states. And photoelectron lifetimes decrease with increasing kinetic energy. To account for these effects in our one-particle scheme, we introduced energy-dependent but spin-independent complex optical potentials for both core holes and photoelectrons. For the optical potentials we used the energy dependence $V_{0i}=a(E-E_0)^b$, the actual parameters $E_0$, $a$, and $b$ being valid only in the energy range of interest. In particular for the core states, this procedure is different from the usual one of calculating the eigenstates for real energies and subsequently broadening the spectra.[54] Second, in order to account for the renormalization of the core-hole Green's function—which is due to correlation and thus computationally demanding—we use an approximative scheme in which exchange splitting and spin-orbit coupling are treated as adjustable parameters and are obtained by adjustment to experiments. Correlation reduces the exchange splitting—a famous example being the Ni valence bands—and thus affects the potential in the core-state region. The latter affects the size of SOC. The exchange splitting can be reduced by scaling the difference of the spin-dependent muffin-tin potentials, a procedure which has proved to give good results for both valence-band photoemission from Ni(001) (Refs. 26 and 27) and core levels.[15] Spin-orbit coupling can be scaled using a quasirelativistic Dirac equation[55–57] which can be regarded as interpolating between the fully relativistic and the scalar-relativistic case.[58–60] In the calculation of the time-reversed low-energy electron diffraction (LEED) state, i.e., the wave function of the photoelectron, SOC and exchange are not scaled because the interaction with the valence $d$ electrons is expected to be rather small at typical kinetic energies. By the above procedure we can take full advantage of our KKR scheme.

We briefly recall some actual parameters for Fe used in the KKR calculations. For emission from Fe $3p$ levels we reduce SOC by a factor of 0.84 and exchange splitting by a factor of 0.48 which differ from those used by Tamura *et al.*[15] (0.6 and 0.4, respectively). The imaginary parts of the optical potentials (lifetime broadenings) are chosen as energy dependent for both core and photoelectron states. For example, the imaginary part is about 4 eV at 110 eV kinetic energy.[61] In order to account for the enhanced surface magnetic moments, we used the correct surface potentials for the three outermost layers, but the bulk potential in the interior. The maximum angular momentum was $l=7$; the number of reciprocal surface-lattice vectors was between 45 and 50.

Excitation processes take place in the 20 outermost layers which is more than sufficient.

## III. ANALYTICAL THEORY OF MAGNETIC DICHROISM FROM ATOMS

In this section, we introduce a simple model of magnetic dichroism from core levels which is mainly based on the works of Menchero,[3] van der Laan,[62] and Goldberg *et al.*[63] Further, a connection to our previous work, Ref. 22, is established. A similar but simpler model has been proposed by Roth.[64]

### A. Core states

For a particular $l$ shell, we introduce the Hamiltonian $H=\lambda\vec{l}\cdot\vec{\sigma}+\zeta\sigma_z$. The first term is the spin-orbit coupling with strength $\lambda$, the second a homogeneous spin field along the $z$ axis.

The Pauli central-field spinors (CFS's) read

$$\Psi_{\kappa\mu}(\vec{r})=R_l(r)\chi_{\kappa\mu}(\hat{r}), \tag{1}$$

where $R_l$ is the radial part and $\chi_{\kappa\mu}$ is a relativistic spin-angular functions (see any textbook on relativistic electron theory, i.e., Ref. 65). The latter are eigenfunctions of $\vec{l}\cdot\vec{\sigma}+1$ with eigenvalue $-\kappa$. Further, we have

$$\langle\chi_{\kappa\mu}|\sigma_z|\chi_{\kappa'\mu'}\rangle=-\frac{2\mu}{2\kappa+1}\delta_{\kappa,\kappa'}\delta_{\mu,\mu'} - \sqrt{1-\left(\frac{2\mu}{2\kappa+1}\right)^2}\,\delta_{\kappa,-\kappa'-1}\delta_{\mu,\mu'}. \tag{2}$$

Thus, $\zeta\sigma_z$ couples states with different $j$ but the same $\mu$. Further, the time-reversal operation $T$ relates $\chi_{\kappa\mu}$ and $\chi_{\kappa,-\mu}$ by $T\chi_{\kappa\mu}=(-1)^{(\mu+1/2)}S_\kappa\chi_{\kappa,-\mu}$, with $S_\kappa=\kappa/|\kappa|$. Due to invariance of the system on rotations around the $z$ axis, $\mu$ is a ''good'' quantum number.

From the above, it follows that eigenfunctions $\Phi_{\kappa\mu}$ of the Hamiltonian can be written as a linear combination of CFS's,

$$\Phi_{\kappa\mu}=c^{(+)}_{\kappa\mu}\Psi_{\kappa\mu}+c^{(-)}_{\kappa\mu}\Psi_{-\kappa-1,\mu}. \tag{3}$$

For $j=l+\frac{1}{2}$ $(\kappa=-l-1)$ and $\mu=\pm(l+\frac{1}{2})$ the eigenenergies are $E_{-l-1,\pm(l+1/2)}=l\lambda\pm\zeta$, from which $\zeta$ can be retrieved (for an experimental attempt see Ref. 66). For the other cases, straightforward calculation leads to

$$E_{\kappa\mu}=-\frac{1}{2}[\lambda+S_\kappa\sqrt{4\zeta(2\mu\lambda+\zeta)+\lambda^2(2l+1)^2}]. \tag{4}$$

For $|2\zeta|\ll(2l+1)\lambda$, the energies are $E_{\kappa\mu}=(-\kappa-1)\lambda-2\mu S_\kappa\zeta/(2l+1)$, which gives a spacing of adjacent levels by $2\zeta/(2l+1)$. For $|2\zeta|\gg(2l+1)\lambda$, we have $E_{\kappa\mu}=-S_\kappa\zeta-\lambda(1+2\mu S_\kappa)/2$ which gives a spacing of adjacent levels by $\lambda/2$ and proves the reversed $\mu$ order of levels which belong to different $\kappa$. Further, magnetization reversal, i.e., turning $\zeta$ into $-\zeta$, interchanges $E_{\kappa\mu}$ and $E_{\kappa,-\mu}$.

We introduce ''reduced'' energies $\tilde{E}_{\kappa\mu}=E_{\kappa\mu}/\alpha$ with the definitions $\lambda=\alpha x$ and $\zeta=\alpha(1-x)$. The dimensionless quantity $x$ can be used to characterize the initial states. Figure 1 shows the dependence of the reduced energies on both SOC and exchange parameters (cf. also Ref. 62).

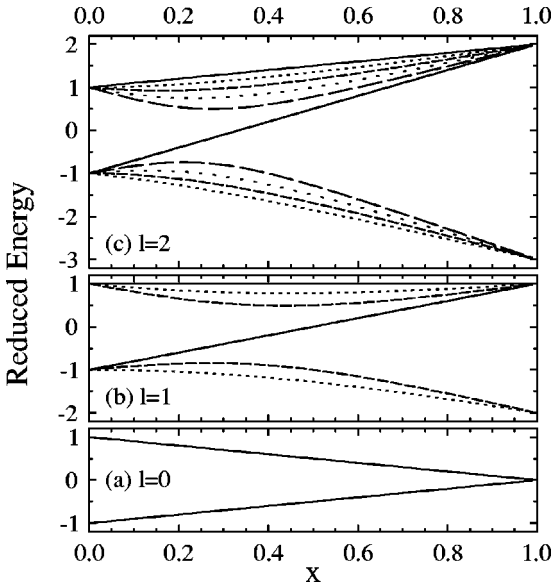


FIG. 1. Reduced energies of initial states for angular momentum $l=0,1,2$ [(a), (b), and (c), respectively] in dependence of spin-orbit coupling $\lambda$ and magnetic exchange $\zeta$. The parameter $x$ is related to $\lambda$ and $\zeta$ by $x=\lambda/(\lambda+\zeta)$. For $x=1$ there is only spin-orbit coupling, for $x=0$ only exchange splitting. Note that $\zeta$ can be retrieved directly from the energy difference of the states with $j=l+1/2$ $(\kappa=-l-1)$ and $\mu=\pm j$ (solid lines). For $\lambda=0$ $(x=0)$ the energies are $\pm\zeta$; for $\zeta=0$ $(x=1)$ they are $l\lambda$ and $-(l+1)\lambda$. Energies of states with equal $\mu$ are represented by identical line styles.

The above results differ qualitatively from that of Tobin *et al.* (cf. in particular Fig. 1 in Ref. 66). In the case of pure SOC $(\zeta=0)$, the number of states with $j=l+\frac{1}{2}$ and $j=l-\frac{1}{2}$ is $2(l+1)$ and $2l$, respectively. For pure exchange $(\lambda=0)$, the number of states for both spin up and down is $2l+1$. Thus, in the transition from pure SOC to pure exchange an odd total number of states has to shift from $j=l+\frac{1}{2}$ $(j=l-\frac{1}{2})$ to pure spin-down (spin-up) states. For example, in our case there is only one $p$ state, namely, with $j=3/2$ and $\mu=-3/2$, shifting, whereas in Tobin's paper there are three. As we will show in Sec. IV A, the energies presented here agree perfectly with those of a numerical calculation, in particular in the case of intermediate strength.

We now address briefly the expansion coefficients $c^{(\pm)}_{\kappa\mu}$ in Eq. (3). For $j=l+\frac{1}{2}$ and $\mu=\pm(l+\frac{1}{2})$, $c^{(-)}_{\kappa\mu}$ is zero because these states do not couple those with $j=l-\frac{1}{2}$ $(\kappa=l)$. For the other states, the calculation of $c^{(\pm)}_{\kappa\mu}$ is straightforward but rather lengthy. In Fig. 2 the coefficients are shown for $p$ initial states $(l=1)$. From $x\approx0.5$ up to $x=1$ the initial states can be regarded as (nearly) pure CFS's; i.e., the absolute values of the coefficients $c^{(+)}$ for $j=3/2$ and $c^{(-)}$ for $j=1/2$ are nearly 1. The compositions for higher angular momenta (not given here) show the same general behavior. The higher the total angular momentum $j$ and its $z$ projection $|\mu|$, the larger the range in which the states can be regarded as pure; e.g., the effect of the spin field can be regarded as small. For example, for $d$ states $(l=2)$, $|c^{(+)}|$ for $j=5/2$ and $|\mu|=3/2$ is greater than 0.9 in the whole range of $x$.

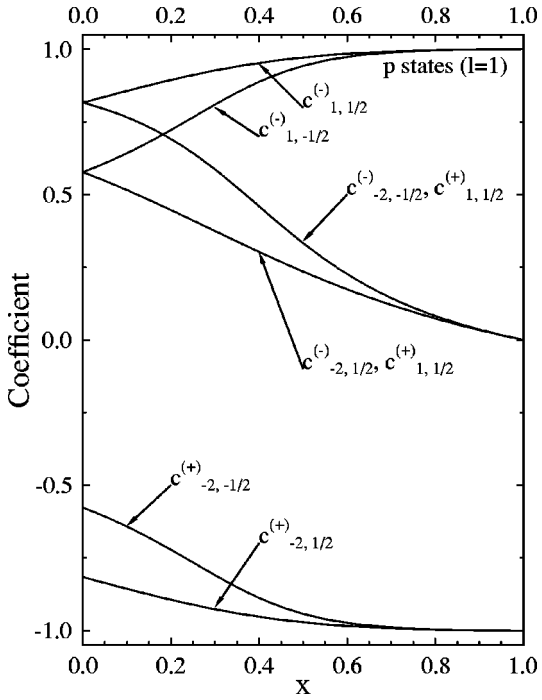


FIG. 2. Composition of $p$ initial states ($l=1$) in dependence of spin-orbit coupling $\lambda$ and magnetic exchange $\zeta$, as represented by the parameter $x$ (see text). For $x=1$ there is only spin-orbit coupling (central field spinors), for $x=0$ only exchange splitting (pure spin states). Only the coefficients $c^{(\pm)}_{\kappa\mu}$ for $\mu=\pm 1/2$ [cf. Eq. (3)] are shown.

### B. Photoelectron states

The photoelectron states are the scattering solutions (continuum states) of electrons propagating in direction of the wave vector $\vec{k}$,

$$\vec{k}=k[\sin\vartheta_e(\vec{e}_x\cos\varphi_e+\vec{e}_y\sin\varphi_e)+\vec{e}_z\cos\vartheta_e], \tag{5}$$

where the polar angle $\vartheta_e$ and the azimuth $\varphi_e$ define the photoelectron detection direction. Note that the $z$ axis is defined by the magnetization direction. Usually one neglects exchange splitting in the photoelectron wave function. Expanded into partial waves, it reads

$$\langle\vec{r}|\Psi_\tau\rangle=4\pi\sum_{lm} i^l e^{-i\delta_l}R_l(r)(Y_l^m(\hat{k}))^\star Y_l^m(\hat{r})\chi^\tau \tag{6}$$

for spin $\tau=\pm 1/2$. Plane waves are recovered by setting the phase shifts $\delta_l$ zero and the radial parts $R_l(r)$ to spherical Bessel functions.

### C. Spin-resolved photoemission

#### 1. Dipole operator

The electric-field vector $\vec{E}$ provides three complex parameters or, equivalently, six real parameters. The normalization condition ($E_x^2+E_y^2+E_z^2=E^2$), the free choice of a general phase, and the assumption that the light impinges within the ($xz$) plane, i.e., $\varphi_{\rm ph}=0$, leaves three parameters: the polar angle of incidence $\vartheta_{\rm ph}$, the ellipticity $\epsilon$ of the field, and the phase $\delta$ between the partial waves within ($E_\parallel$) and perpendicular ($E_\perp$) to the ($xz$) plane (cf. Fig. 3). Linear (circular) polarized light is characterized by $\delta=0$ and $\epsilon=0,\pi/2$ ($\delta=\pm\pi/2$ and $\epsilon=\pi/4$). With the definitions

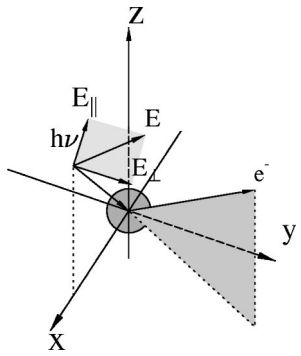


FIG. 3. Geometry used in the analytical calculations. The grey circle represents the atom with magnetic moment along the $z$ direction. Light ($h\nu$) impinges within the ($xz$) plane, its electric-field vector $E$ being decomposed into a part within ($E_\parallel$) and perpendicular ($E_\perp$) to the incidence plane. Electrons ($e^-$) are detected in a general direction.

$$E_\pm=\frac{E}{\sqrt{2}}(\cos\vartheta_{\rm ph}\cos\epsilon\, e^{i\delta}\mp i\sin\epsilon), \tag{7a}$$

$$E_0=-E\sin\vartheta_{\rm ph}\cos\epsilon\, e^{i\delta}, \tag{7b}$$

the dipole operator reads

$$\vec{E}\cdot\vec{r}=\sqrt{\frac{4\pi}{3}}r[-E_+Y_1^1(\hat{r})+E_0Y_1^0(\hat{r})+E_-Y_1^{-1}(\hat{r})]. \tag{8}$$

#### 2. Density matrix

The density matrix of the photoelectron originating from initial state $\Phi_{\kappa\mu}$ has elements $\varrho_{\kappa\mu\tau\tau'}=M_{\kappa\mu\tau}(M_{\kappa\mu\tau'})^\star$, with the transition matrix elements defined by $M_{\kappa\mu\tau}=\langle\Psi_\tau|\vec{E}\cdot\vec{r}|\Phi_{\kappa\mu}\rangle$. The intensity is $I_{\kappa\mu}=\mathrm{tr}(\varrho_{\kappa\mu})$, the electron spin polarization (ESP) $\vec{P}_{\kappa\mu}=\mathrm{tr}(\vec{\sigma}\varrho_{\kappa\mu})/I_{\kappa\mu}$ with the vector of Pauli matrices, $\vec{\sigma}$.

In valence-band photoemission, each element of the density matrix consists of two terms, one for each member of a Kramers doublet,[22] because in general in the valence bands for each initial-state energy there are these two eigensolutions of the Hamiltonian. In the atomic core-level regime, discrete energy levels imply that for a given initial-state energy there is only one eigensolution and thus, only one term in $\varrho$.

#### 3. Transition-matrix elements

The angular matrix elements $I_{lnl'}^{m\nu m'}$, which appear due to the integration over angles in the matrix elements $M_{\kappa\mu\tau}$, can be written as a product of two Clebsch-Gordan coefficients.[67] One obtains for $n=1$ and $\nu=\pm 1$

$$I_{l1l'}^{m,\pm 1,m'}=\sqrt{\frac{3}{8\pi}}\left(-\sqrt{\frac{(l\mp m+1)(l\mp m+2)}{(2l+1)(2l+3)}}\delta_{l',l+1}+\sqrt{\frac{(l\pm m-1)(l\pm m)}{(2l-1)(2l+1)}}\delta_{l',l-1}\right)\delta_{m',m\mp 1} \tag{9}$$

and for $n=1$ and $\nu=0$

$$I_{l1l'}^{m0m'}=\sqrt{\frac{3}{4\pi}}\left(\sqrt{\frac{(l-m+1)(l+m+1)}{(2l+1)(2l+3)}}\delta_{l',l+1}+\sqrt{\frac{(l-m)(l+m)}{(2l-1)(2l+1)}}\delta_{l',l-1}\right)\delta_{mm'}. \tag{10}$$

These results state the very well-known selection rule $\Delta l=\pm 1$. For the matrix elements $D_{ll'}^{mm'}$ of the dipole operator, Eq. (8), we obtain eventually

$$D_{ll'}^{mm'}=\int_\Omega (Y_l^m)^\star(\vec{E}\cdot\vec{r})Y_{l'}^{m'}\,d\Omega$$

$$=\sqrt{\frac{4\pi}{3}}r(-E_+I_{l1l'}^{m1m'}+E_0I_{l1l'}^{m0m'}+E_-I_{l1l'}^{m,-1,m'}). \tag{11}$$

$E_\pm$ mediates transitions from initial states with magnetic quantum number $m$ into partial waves with $m\pm 1$, whereas $E_0$ implies transitions between states with equal $m$.

With the definition

$$T_{l'l}^m=\tilde{R}_{l'l}\sum_{m'} Y_{l'}^{m'}(\hat{k})D_{l'l}^{m'm}, \tag{12}$$

the radial matrix elements

$$\tilde{R}_{l'l}=\exp(i\delta_{l'})\int r^3R_{l'}(r)R_l(r)dr, \tag{13}$$

and using spin conservation within the excitation process, the matrix elements of the dipole operator between a CFS, Eq. (1), and a photoelectron state $|\Psi_\tau\rangle$, Eq. (6), read

$$\langle\Psi_\tau|\vec{E}\cdot\vec{r}|\kappa\mu\rangle=4\pi(-i)^{l-1},$$

$$C\left(l\,\frac{1}{2}\,j;\mu-\tau,\tau\right)(T_{l-1,l}^{\mu-\tau}-T_{l+1,l}^{\mu-\tau}). \tag{14}$$

Eventually, one arrives at the matrix elements $M_{\kappa\mu\tau}$,

$$M_{\kappa\mu\tau}=c_{\kappa\mu}^{(+)}\langle\Psi_\tau|\vec{E}\cdot\vec{r}|\Psi_{\kappa\mu}\rangle+c_{\kappa\mu}^{(-)}\langle\Psi_\tau|\vec{E}\cdot\vec{r}|\Psi_{-\kappa-1,\mu}\rangle. \tag{15}$$

Radial matrix elements and phase shifts $\delta_l$ are listed for typical photon energies in Ref. 63. In principle, all ingredients for the photoemission calculations have now been presented.[68]

### D. Magnetic circular and linear dichroism

At last, we address briefly basics properties of magnetic circular dichroism (MCD) and magnetic linear dichroism (MLD) in their standard setups.

#### *1. Magnetic circular dichroism*

The standard setup for MCD is given by incidence of circular polarized light ($\epsilon=\pi/4$, $\delta=\pm\pi/2$) along the magnetization direction ($z$ axis, $\vartheta_{\rm ph}=0$) and arbitrary electron-detection direction. The angular matrix elements $D_{l\pm1,l}^{m,m'}$ consist of only one term because $E_+=0$ ($E_-=0$) and $E_-=i$ ($E_-=-i$) for $\sigma+$ ($\sigma-$) light. In both cases $E_0$ vanishes.

Due to the symmetry of the setup, the intensity does not depend on the detection azimuth $\varphi_e$. Thus, without loss of generality we can assume detection within the $(xz)$ plane ($\varphi_e=0$). Reflection at the $(xy)$ plane turns $\vartheta_e$ into $-\vartheta_e$ and gives the relation

$$(I,P_x,P_y,P_z)\ \overset{\vartheta_e\to\pi-\vartheta_e}{\to}\ (I,-P_x,-P_y,P_z), \tag{16}$$

which for $\vartheta_e=\pi/2$ yields $P_x=P_y=0$. Reflection at the $(xz)$ plane reverses both the helicity of the light and the magnetization and gives the relation

$$(I,P_x,P_y,P_z)\ \overset{(\sigma_\pm,\vec{M})\to(\sigma_\mp,-\vec{M})}{\to}\ (I,-P_x,P_y,-P_z). \tag{17}$$

For $\vartheta_e=0$ we have also $P_x=P_y=0$ due to the rotational invariance of the system (cf. Ref. 69).

For $\zeta=0$, it can be shown that the dichroism defined by $\Delta_{\kappa\mu}=I_{\kappa\mu}-I_{\kappa,-\mu}$, $\mu>0$, can be written as $f_{\kappa\mu}\Delta_l$. Thus, the dichroism can be separated into a geometric ($\Delta_l$) and an orbital part ($f_{\kappa\mu}$). The factor $f_{\kappa\mu}$ for $l>0$ is only nonzero for $\mu=\frac{1}{2},\frac{3}{2}$ with values $S_\kappa(\kappa+2-2\mu)$. For $p$ states, this restates the well-known results $\Delta_{-2,3/2}=3\Delta_1$, $\Delta_{-2,1/2}=\Delta_1$, and $\Delta_{1,1/2}=2\Delta_1$.

#### *2. Magnetic linear dichroism*

The standard setup for MLD is given by incidence of linear polarized light ($\epsilon=\pi/2$, $\delta=0$) perpendicular to the magnetization direction ($\vartheta_{\rm ph}=\pi/2$) and arbitrary electron-detection direction. This leads to $E_\pm=\mp iE/\sqrt{2}$ and again $E_0=0$. Thus, the angular matrix elements $D_{l\pm1,l}^{m,m'}$ comprise the sum of $I_{l\pm1,1,l}^{m1m'}$ and $I_{l\pm1,1,l}^{m,-1,1m'}$ and therefore relate MLD to MCD.

Contrary to MCD, the intensity does now depend on the azimuth $\varphi_e$. Reflection at the $(xy)$ plane gives the relations

$$(I,P_x,P_y,P_z)\ \overset{\vartheta_e\to\pi-\vartheta_e}{\to}\ (I,-P_x,-P_y,P_z), \tag{18}$$

which states $P_x=P_y=0$ for $\vartheta_e=\pi/2$. Reflection at the $(xz)$ plane reverses the magnetization, turns $\varphi_e$ into $-\varphi_e$, and gives the relation

$$(I,P_x,P_y,P_z)\ \overset{(\varphi_e,\vec{M})\to(-\varphi_e,-\vec{M})}{\to}\ (I,-P_x,P_y,-P_z). \tag{19}$$

Further, reflection at the $(yz)$ plane yields

$$(I,P_x,P_y,P_z)\ \overset{(\varphi_e,\vec{M})\to(\pi-\varphi_e,-\vec{M})}{\to}\ (I,P_x,-P_y,-P_z). \tag{20}$$

Equations (19) and (20) state the well-known result that MLD can be either observed by reversing the magnetization or reversing the detection azimuth. Obviously, there is no MLD if $\varphi_e=0$, Eq. (19), or if $\varphi_e=\pi/2$, Eq. (20).

The above symmetry relations confirm the ''general rule'' of magnetic dichroism. In all setups where there is MLD,

there is a nonvanishing ESP component along the magnetization (here $P_z$) in the nonmagnetic limit. And in the nonmagnetic cases with $P_z=0$, there is no MLD in the same setup with nonzero $\vec{M}$. For standard MCD, $P_z$ is always nonzero in the nonmagnetic case; thus there is MCD for all polar angles of detection.

## IV. RESULTS AND DISCUSSION

In this section, our results will be presented, discussed, and compared with experiment for the prototypical case of photoemission from Fe $3p$ levels. We address MCD (Sec. IV B), ''double dichroism'' (Sec. IV C), and diffraction effects in off-normal emission (Sec. IV D) from Fe(001) as well as MLD from Ni(110) (Sec. IV E). However, before turning to photoemission, we consider the applicability of the analytical theory presented in Sec. III.

### A. Comparison of numerical with analytical calculations

In this subsection, we check whether energies and wave functions of core levels, which have been obtained by solving the Dirac equation for a site potential, can be successfully reproduced by those obtained from the simple model Hamiltonian (cf. Sec. III).

The $2p$ levels of Fe in the bulk show relative energies of $-8.47$ eV, $-8.15$ eV, 3.67 eV, 4.01 eV, 4.34 eV, and 4.65 eV as obtained by KKR for the ground state (without scaling SOC and exchange splitting). These energies can excellently be reproduced by the analytical expression, Eq. (4), with SOC $\lambda=8.30$ eV and exchange energy $\zeta=0.98$ eV (see Fig. 4). Thus, the quantity $x=\lambda/(\lambda+\zeta)$ used in Fig. 1 is 0.89; i.e., we are concerned with strong SOC ($\lambda \gg \zeta$) which groups the six levels into two groups with two ($j=1/2$) and four ($j=3/2$) states. The splitting of the $2p$ levels presented in Ref. 70 is 13.1 eV which is slightly larger than the average splitting of 12.5 eV in our calculations. Further, the ratio $\zeta/\lambda=0.12$ agrees very well with that given by van der Laan[62] (0.1).

The bulk $3p$ levels show relative energies of $-1.92$ eV, $-1.48$ eV, $-0.71$ eV, 0.95 eV, 1.39 eV, and 1.73 eV which lead to $\lambda=1.04$ eV and $\zeta=2.44$ eV ($x=0.30$). Here, exchange is rather strong compared to SOC and the grouping of levels—as obtained for the $2p$ states—does not exist. In order to reproduce the experimental photoemission spectra, we used scaled values of $\lambda=0.87$ eV and $\zeta=1.17$ eV (cf. Sec. II), thus enhancing $x$ to 0.56. The ratio $\zeta/\lambda=1.35$ agrees well with that given by van der Laan[62] (1.37 from Hartree-Fock theory). Hillebrecht and co-workers[71] obtained by fitting to their experimental results $\lambda=0.94$ eV and $\zeta=0.99$ eV ($x=0.49$) for Fe $3p$ which compare quite well with ours. The rather small deviations might be explained by the experimental resolution which does not allow an identification of the spin-orbit split core levels (cf. also Ref. 70). However, their assumption of equidistant spacing of the energy levels is rather crude and not confirmed by either our analytical or our numerical calculations (cf. Fig. 1).

The spin-orbit coupling strength is proportional to the gradient of the potential which explains why $\lambda$ of the $2p$ shell is by far larger than that of the $3p$ shell. The exchange splitting

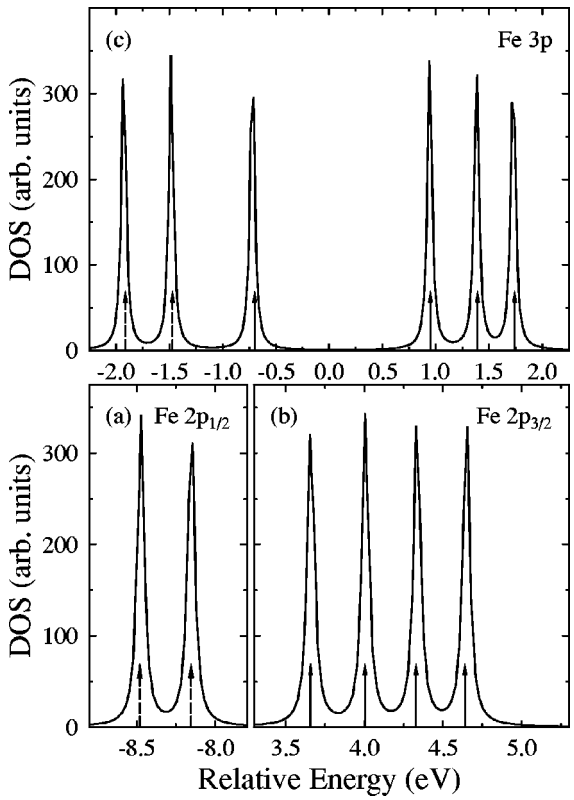


FIG. 4. Density of states of Fe $2p$ [bottom panels (a), (b)] and Fe $3p$ [upper panel, (c)] levels as obtained by the KKR calculations. Vertical dashed and solid arrows mark relative energy positions of the respective states with $j=1/2$ and $j=3/2$, respectively, obtained within the analytical theory.

of the core levels is due to the interaction of the former with the spin-polarized valence electrons and thus depends also on the shell [$\zeta(3p)>\zeta(2p)$]. Further, the energy positions obtained by scaling the SOC and exchange in the KKR calculations can be easily obtained within the analytical theory by scaling $\lambda$ and $\zeta$ by the same factors as used in the KKR scheme. And last, the fitting of peak positions to experimental data is simplified by using the analytical expression, Eq. (4), because the number of adjustable parameters is reduced from 6 (each for one level) to 3 ($\lambda$, $\zeta$, and a rigid energy shift).

As a second check, we have calculated the density of states (DOS) projected on spherical harmonics $Y_1^m$ times a Pauli spinor $\chi^\tau$, $\tau=\pm$, for each Fe $2p$ and Fe $3p$ state using the layer-resolved KKR Green's function $G$:

$$N_{1m\tau}(E)=-\frac{1}{\pi}\lim_{\eta\to 0_+}\mathrm{Im}\,G_{1m\tau,1m\tau}(E+i\eta). \qquad (21)$$

The corresponding weights can also be obtained from Eq. (1) using Clebsch-Gordan coefficients and the parameters $\lambda$ and $\zeta$. The norm of the radial part of the wave functions appears as a common factor when comparing numerical with analytical theory. The relative contributions to the DOS are given in Tables I and II for the two components in the analytical theory. We find a perfect agreement between numerical and analytical calculations which gives strong evidence that the analytical theory not only applies to the case of weak exchange ($\zeta \ll \lambda$), but also to the whole coupling range. Fur-

TABLE I. Partial density of states of Fe $3p$ states $\Psi_{\kappa\mu}$ as obtained by KKR and analytical calculations. The relative energy is given in the second column. In the analytical theory, each state consists of only two components (spherical harmonics $Y_1^m$ times Pauli spinor $\chi^\tau$, $\tau=\pm$) the indices of which are given in columns 4 and 7 $(m,\tau)$, the associated normalized weights in columns 6 and 9 (Ana.). Their numerical counterparts are shown in columns 5 and 8 (KKR).

| $\kappa$ | $\mu$ | Energy | $m,\tau$ | KKR | Ana. | $m,\tau$ | KKR | Ana. |
|---|---|---|---|---|---|---|---|---|
| 1 | 1/2 | −1.92 eV | −1,+: | 0.051 | 0.052 | 0,−: | 0.948 | 0.948 |
| 1 | −1/2 | −1.48 eV | 0,+: | 0.101 | 0.103 | 1,−: | 0.898 | 0.897 |
| −2 | −3/2 | −0.71 eV | −1,−: | 0.999 | 1.000 | — | — | — |
| −2 | −1/2 | 0.95 eV | −1,+: | 0.899 | 0.897 | 0,−: | 0.101 | 0.103 |
| −2 | 1/2 | 1.39 eV | 0,+: | 0.947 | 0.948 | 1,−: | 0.051 | 0.052 |
| −2 | 3/2 | 1.73 eV | 1,+: | 0.999 | 1.000 | — | — | — |

ther, this agreement supports that the radial wave functions for the $(j=1/2)$ and $(j=3/2)$ states can be taken as identical, as is usually done.[3,63]

In conclusion, the rather simple Hamiltonian (see Sec. III A) in conjunction with Pauli central-field spinors as basis functions appears to be appropriate when describing both energy eigenvalues and wave functions of Fe $p$ core levels. We would like to note that $3p$ states of Co and Ni are also very well described. Photoemission results for Fe $3p$ and Ni $3p$ will be presented in Secs. IV D and IV E.

### B. Magnetic circular dichroism from Fe(001)

Magnetic circular dichroism experiments with and without spin resolution from $3p$ levels of Fe(001) have been performed by Hillebrecht *et al.*[71] The magnetization $\vec{M}$ was along [100] and circularly polarized light impinged quasiparallel to $\vec{M}$ with polar angle $\vartheta_{\rm ph}=74°$ onto the surface. Electrons were detected in normal emission.

Before turning to the photoemission intensities we address the energy positions of the core states; cf. Fig. 5. Both the spin-orbit coupling strength λ and the exchange splitting $\zeta$ have been reduced in order to reproduce the background-corrected experimental spectra (not shown here). The obtained energy positions of the Fe $3p$ states are shown in Fig. 5 as vertical arrows. Sirotti and Rossi[72,73] obtained the following energies by fitting to their experimental spectra: −52.2 eV, −52.5 eV, −52.9 eV, −53.3 eV, −53.9 eV, and −54.8 eV. In particular, the two latter values appear too high in binding energy as compared to our values which may be due to difficulties in fitting the low-energy and low-

TABLE II. Same as Table I, but for Fe $2p$ states.

| $\kappa$ | $\mu$ | Energy | $m,\tau$ | KKR | Ana. | $m,\tau$ | KKR | Ana. |
|---|---|---|---|---|---|---|---|---|
| 1 | 1/2 | −8.47 eV | −1,+: | 0.699 | 0.700 | 0,−: | 0.300 | 0.300 |
| 1 | −1/2 | −8.15 eV | 0,+: | 0.369 | 0.370 | 1,−: | 0.630 | 0.630 |
| −2 | −3/2 | 3.67 eV | −1,−: | 0.999 | 1.000 | — | — | — |
| −2 | −1/2 | 4.01 eV | −1,+: | 0.299 | 0.300 | 0,−: | 0.698 | 0.700 |
| −2 | 1/2 | 4.34 eV | 0,+: | 0.630 | 0.630 | 1,−: | 0.369 | 0.370 |
| −2 | 3/2 | 4.65 eV | 1,+: | 0.998 | 1.000 | — | — | — |

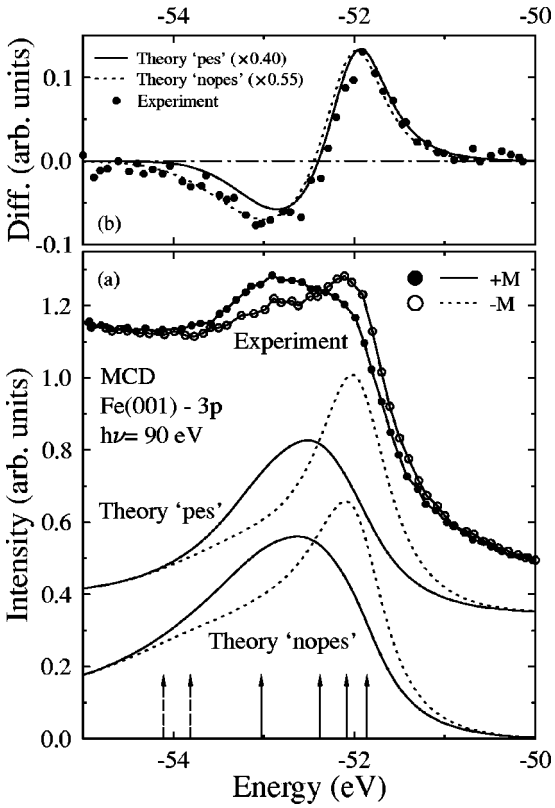


FIG. 5. Magnetic circular dichroism (MCD) in normal emission of Fe $3p$ levels at Fe(001) with 90 eV photon energy. (a) Theoretical intensities without (bottom, ''nopes'') and with (middle, ''pes'') photoelectron scattering compared to experimental ones (top, reproduced from Ref. 71) for magnetization direction $+\vec{M}$ (solid lines, solid circles) and $-\vec{M}$ (dotted lines, open circles). The experimental spectra are not corrected for incomplete light polarization and inelastic background. Vertical arrows represent energy positions of theoretical core levels. (b) Intensity differences of the intensities shown in panel (a). Theoretical ''pes'' spectra are scaled in order to obtain the experimental value at −51.9 eV without background correction.

intensity edge of the spectra. Further, such a large energy splitting is not compatible with either our analytically or our numerically obtained splittings (cf. Fig. 1). It would be desirable to use a fitting procedure using the analytically obtained peak positions in order to reduce the number of free parameters.

Now we turn to the spin-averaged dichroic intensities [Fig. 5(a)]. Due to the energy-dependent lifetime broadening, the theoretical intensities are reduced for higher binding energies (for the core-hole we choose $a=0.07$, $E_0=-49.5$ eV, and $b=2$, for the photoelectron $a=1.8$ and $b=0$). This suppresses the dichroism in the energy range of the states with $j=1/2$ [dashed arrows in Fig. 5(a)] which is usually present in atomic calculations (see, for example, Ref. 62). In other words, the dichroism can be regarded as mainly due to initial states with $j=3/2$ [solid arrows in Fig. 5(a)]. Scattering within the photoelectron state [''pes,'' middle spectra in Fig. 5(a)] leads to an increase in the overall intensity by roughly a factor of 2 compared to spectra without scattering (''nopes,'' bottom spectra). Further, the intensity relations between single lines have slightly changed. This leads—besides a strong increase—to a shift of about 0.05 eV

to higher energies in the intensity differences [Fig. 5(b); cf. the maxima at about $-51.9$ eV]. This means that photoelectron scattering leads to a slight change in the dichroic signal in both shape and energy position, which is rather typical since turning from the ''nopes'' case to the ''pes'' case changes the density of states of the upper states. We would like to note that the above scattering effects on the dichroism become much larger if the lifetime broadening is reduced.

Comparing the theoretical ''pes'' spectra with their experimental counterparts, we observe good agreement in both the general shape and the dichroism. In theory, the intensity difference is in general larger than in experiment due to incomplete light polarization as well as energetic and angular resolution in the latter. In particular, the difference minimum at $-52.9$ eV is not as deep in experiment as it is in theory. Further, the intensity ratios of the maxima at $-52.0$ eV $(-\vec{M})$ and $-52.6$ eV $(+\vec{M})$ agree well with the background-corrected experimental data (not shown here).

The general behavior of the intensities under magnetization reversal can easily be explained within the atomic model. Starting in the limit of weak exchange splitting ($\zeta \ll \lambda$, $x \approx 1$), one observes that the dichroism can be split into an orbital and a geometrical part (see Sec. III D 1). As we have seen above, this limit cannot be applied in a correct description of the Fe $3p$ states ($\lambda = 0.87$ eV, $\zeta = 1.17$ eV). Thus, the dichroism of the core states with $\mu = \pm 1/2$ does not follow the simple rule derived in Sec. III D 1, but appears to be more complicated due to the mixing of central-field spinors with $j = 1/2$ and $j = 3/2$ with weights $c^{(+)}$ and $c^{(-)}$. Core states with $\mu = \pm 3/2$ are of course not affected.

After having described successfully the spin-averaged experimental spectra, we now turn to spin-resolved dichroic spectra [cf. Figs. 6(a) and 6(c)] which have been recorded in the same geometry as the spin-averaged ones. We recall that the light impinges with 74° polar angle onto the surface which induces spin-polarization components normal to the surface (along [001]) and within the surface plane but normal to the magnetization direction (along [010]). However, these are rather small (less than 10% in absolute value) compared to the component parallel to the magnetization ([100]).

For helicity $\sigma+$ [Fig. 6(a)], we find in theory a distinct energetic separation of states with majority and minority spin character, as expected from atomic theory. The former can be attributed to the three states with highest binding energy, the latter to the other three states. In the intensity differences [Fig. 6(b)] this leads to a $+/-$ shape. Both maxima show approximately the same height. The experiment, however, shows that the minority intensity is larger than the majority intensity in the whole energy range presented here. Thus, in the difference spectrum only a minimum occurs. Turning to helicity $\sigma-$ [Figs. 6(c) and 6(d)], we observe a strong increase in the minority intensity compared to the $\sigma+$ case. The majority intensity is rather structureless and weak. Further the position of the minority maximum has shifted to higher energies. In the difference [Fig. 6(d)] we find the minimum around $-52.0$ eV dominating; the maximum at $-53.1$ eV has become broad and very weak. In experiment, the above increase is also observed but appears not as pronounced as in theory. In summary, our theory is able to reproduce the trends observed in experiment.

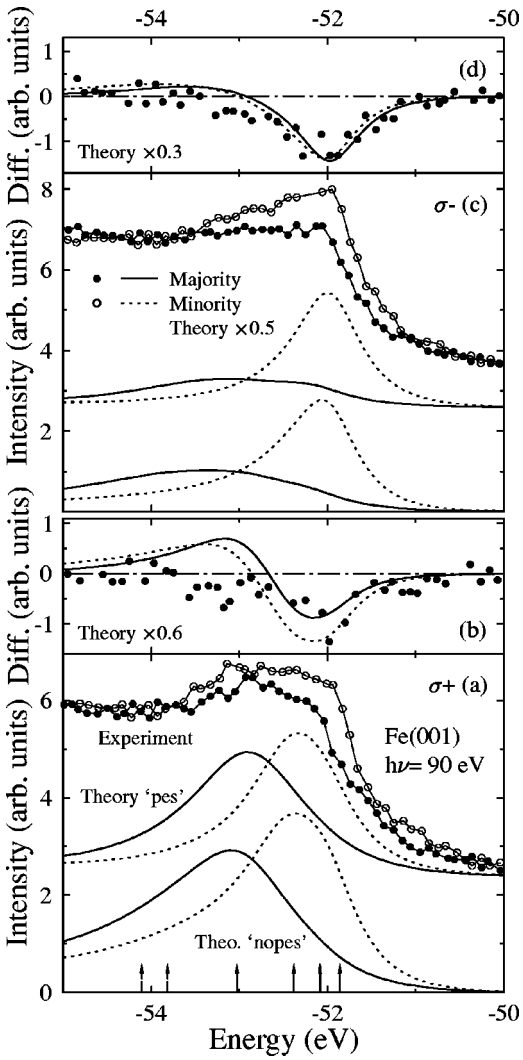


FIG. 6. Spin-resolved normal photoemission with circularly polarized light of Fe $3p$ levels at Fe(001) with 90 eV photon energy. (a) Theoretical spectra without (bottom, ''nopes'') and with (middle, ''pes'') photoelectron scattering compared to their experimental counterparts (top, reproduced from Ref. 71) for helicity $\sigma+$. Majority (minority) spectra are shown as solid (dotted) lines and solid (open) circles. Vertical arrows denote theoretical energy positions of the $3p$ states. (b) Differences of the experimental (solid circles) and theoretical (''nopes'' dotted line, ''pes'' solid line) intensities of panel (a). (c) and (d) As in panels (a) and (b), respectively, but for helicity $\sigma-$.

Scattering in the photoelectron state leads to changes in the spin polarization, which are most significant for helicity $\sigma+$. In particular, the energy position of the sign change is shifted from $-52.9$ eV up to $-52.7$ eV.

The spin polarization of the photoelectrons is due to both optical orientation and exchange splitting. Obviously, the SOC-induced spin polarization does not depend on magnetization reversal; the exchange-induced one does not depend on light-polarization reversal. Thus, by averaging over the sample magnetization directions, one obtains the spin-orbit induced spin polarization and the respective spin-resolved intensities $\tilde{I}_{\pm}$,

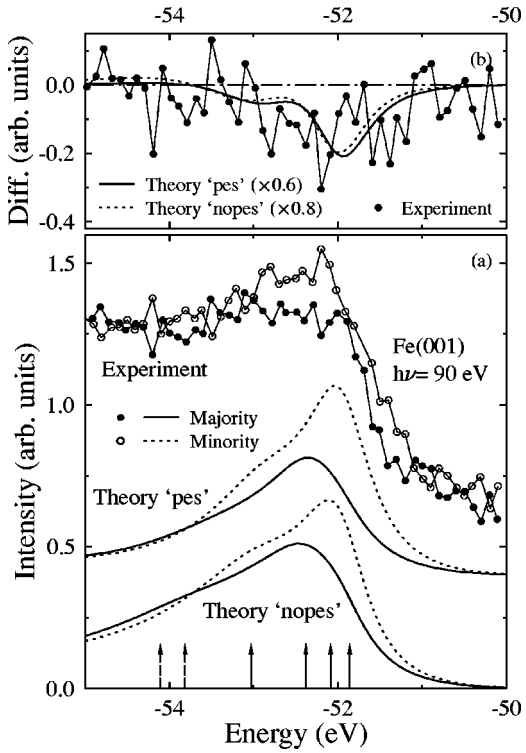


FIG. 7. Spin-resolved normal photoemission with circularly polarized light of Fe $3p$ levels at Fe(001) with 90 eV photon energy. (a) Theoretical spectra without (bottom, ''nopes'') and with (middle, ''pes'') photoelectron scattering compared to their experimental counterparts (top, circles, reproduced from Ref. 71). Majority (minority) spectra according to Eq. (22) are shown as solid (dotted) lines or solid (open) circles, respectively. Vertical arrows denote theoretical energy position of the $3p$ states. (b) Intensity differences of the spectra of panel (a).

$$\tilde{I}_+ = I_+(\sigma+) + I_-(\sigma-), \tag{22a}$$

$$\tilde{I}_- = I_+(\sigma-) + I_-(\sigma+). \tag{22b}$$

In Fig. 7(a), we compare theoretical intensities $\tilde{I}$ with their experimental counterparts. In all three cases, the minority intensity exceeds the majority intensity which leads to a minimum in the intensity differences [Fig. 7(b)]. This behavior can be explained easily within the theory: the minority maximum for helicity $\sigma-$ is much larger than the minority maximum for helicity $\sigma+$. Further, the majority maximum for helicity $\sigma-$ is much larger than the majority maximum for helicity $\sigma+$ (cf. Fig. 6).

A theoretical calculation based on atomic theory[64] shows a $+/-$ shape of the intensity difference (Fig. 3 in Ref. 71) and thus fails to describe the experimental findings [Fig. 7(b)]. It relies on a spin-orbit coupling strength which is by far larger than exchange splitting, equidistant energy spacing of the initial-state energies, and energy-independent lifetime broadening. From our analysis it is evident that spin-orbit coupling strength and exchange splitting of approximately the same magnitude in conjunction with energy-dependent lifetime broadening should be applied in order to reproduce the experimental results. Photoelectron scattering appears to be of minor importance [cf. Fig. 7(b)].

In conclusion, we have successfully described MCD from $3p$ levels of Fe(001). Scattering in the photoelectron state at normal emission influences both intensity and spin polarization mildly, but should be taken into account in theory.

### C. Double dichroism

In a previous study, we have analyzed magnetic dichroism in a chiral setup in photoemission from valence bands.[24] The combination of circular dichroism in angular distribution (CDAD)—which is present already in photoemission from nonmagnetic surfaces—with magnetic dichroism yields so-called ''double'' dichroism: the photocurrent does now depend on reversal of both the magnetization direction and the helicity. Thus, there are now four different intensities $I(\sigma\pm, \pm\vec{M})$. In a nonchiral setup, for example in normal emission, the relation $I(\sigma\pm, \pm\vec{M}) = I(\sigma\mp, \mp\vec{M})$ yields only two different spectra. A chiral setup breaks this symmetry relation. Further, we have shown how both effects—the photoelectron-related CDAD effect due to interference of the outgoing partial waves and the magnetic initial-state effect—can be separated. We now turn to double dichroism in core-level photoemission.

As a prototypical chiral setup we choose—as in the previous subsection—Fe(001) with magnetization $\vec{M}$ along [100] ($x$). Circularly polarized light impinges—as in the MCD experiments and calculations in the previous section quasiparallel to $\vec{M}$—in the [100] azimuth with polar angle $\vartheta_{\mathrm{ph}} = 74°$. Electrons are detected in the [010] azimuth under a polar angle of $\vartheta_e = 5°$. Reflection at the (010) plane yields the symmetry relation $I(\sigma+, +\vec{k}_\parallel, +\vec{M}) = I(\sigma-, -\vec{k}_\parallel, -\vec{M})$. Thus, we calculated four intensities with the magnetization kept fixed, $I(\sigma\pm, \pm\vec{k}_\parallel)$.

In order to separate the CDAD and MCD effects, we define the asymmetries

$$A_{\mathrm{pol}} = [I(\sigma+, +\vec{k}_\parallel) + I(\sigma-, -\vec{k}_\parallel) - I(\sigma+, -\vec{k}_\parallel) - I(\sigma-, +\vec{k}_\parallel)]/I_0, \tag{23a}$$

$$A_{\mathrm{mag}} = [I(\sigma+, +\vec{k}_\parallel) - I(\sigma-, -\vec{k}_\parallel) - I(\sigma+, -\vec{k}_\parallel) + I(\sigma-, +\vec{k}_\parallel)]/I_0, \tag{23b}$$

$$A_{\mathrm{ex}} = [I(\sigma+, +\vec{k}_\parallel) - I(\sigma-, -\vec{k}_\parallel) + I(\sigma+, -\vec{k}_\parallel) - I(\sigma-, +\vec{k}_\parallel)]/I_0, \tag{23c}$$

with the averaged intensity $I_0 = I(\sigma+, +\vec{k}_\parallel) + I(\sigma-, -\vec{k}_\parallel) + I(\sigma+, -\vec{k}_\parallel) + I(\sigma-, +\vec{k}_\parallel)$. With the above symmetry relation, it is obvious that $A_{\mathrm{pol}}$ averages over the magnetization and thus retrieves the (''nonmagnetic'') CDAD effect. $A_{\mathrm{mag}}$ averages out the dependence on the light helicity and thus yields the pure effect of unpolarized light. And last, $A_{\mathrm{ex}}$ reveals the MCD.

In Fig. 8(a), the four intensities are shown. With scattering in the photoelectron state (''pes''), all four spectra differ significantly from each other. Without photoelectron scattering (''nopes''), however, we observe that two intensities are nearly equal, $I(\sigma\pm, +5°) \approx I(\sigma\pm, -5°)$. If they were iden-

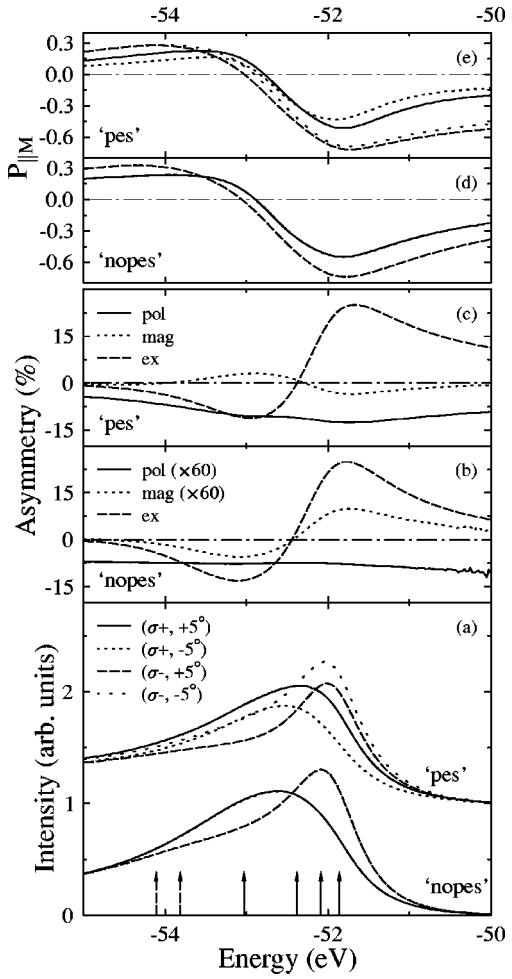


FIG. 8. Circular ''double'' dichroism from $3p$ levels of Fe(001) at 90 eV photon energy and 5° off-normal emission. (a) Intensities from calculations without (''nopes,'' bottom) and with (''pes,'' top) photoelectron scattering for two light helicities ($\sigma\pm$) and detection angles ($\pm 5°$). Vertical arrows denote the $3p$ energy levels. (b) and (c) Asymmetries as defined in Eq. (23). In the ''nopes'' case (b), $A_{\mathrm{pol}}$ and $A_{\mathrm{mag}}$ are scaled by factors 60 and 30, respectively. (d) and (e) Photoelectron spin polarizations parallel to the magnetization. Line styles as indicated in panel (a).

tical, e.g., due to the existence of a symmetry operation which connects the respective setups, $A_{\mathrm{pol}}$ and $A_{\mathrm{mag}}$ would vanish, and $A_{\mathrm{ex}}$ would remain nonzero. This is shown in Fig. 8(b) (note the factors for $A_{\mathrm{pol}}$ and $A_{\mathrm{mag}}$) which indicates that CDAD is due to photoelectron scattering. The polarization induced asymmetry (CDAD) in the ''pes'' case is nearly constant throughout the energy range presented here, with an average value of about $-7.5\%$. Its magnetization-induced partner $A_{\mathrm{mag}}$ shows a $+/-$ shape with maximal absolute value of 3%. The exchange-induced asymmetry compares in shape well that for normal emission (Fig. 5) and is rather mildly affected by photoelectron scattering. In summary, the above proves that the photoelectron effect (CDAD) can be separated from the initial-state effect (MCD). At last, we like to mention that the spin-polarization component parallel to the magnetization [Figs. 8(d) and 8(e)] shows the same behavior as the intensities regarding the effect of photoelectron scattering.

As the sum of circularly polarized light with left- and right-handed helicity can be regarded as the incoherent sum of *s*- and off-normally incident *p*-polarized light, it follows that the relation

$$I(\sigma+,\pm\vec{k}_{\|})+I(\sigma-,\pm\vec{k}_{\|})=I(s,\pm\vec{k}_{\|})+I(p,\pm\vec{k}_{\|}) \quad (24)$$

holds. From the ''general rule'' of dichroism—if in the nonmagnetic limit a spin-polarization component along [100] (i.e., aligned to $\vec{M}$) is produced, then there is magnetic dichroism—it is evident that both the *s*-polarized and *p*-polarized parts of the light create dichroism in a chiral setup. In normal emission, however, the ESP component parallel to $\vec{M}$ vanishes in the nonmagnetic limit and, thus, there is no MD. According to Eq. (23) we define corresponding asymmetries for *s*- and *p*-polarized light,

$$\tilde{A}_{\mathrm{pol}}=[I(s,+\vec{k}_{\|})-I(p,+\vec{k}_{\|})+I(s,-\vec{k}_{\|})-I(p,-\vec{k}_{\|})]/I_0, \quad (25a)$$

$$\tilde{A}_{\mathrm{mag}}=[I(s,+\vec{k}_{\|})+I(p,+\vec{k}_{\|})-I(s,-\vec{k}_{\|})-I(p,-\vec{k}_{\|})]/I_0, \quad (25b)$$

$$\tilde{A}_{\mathrm{ex}}=[I(s,+\vec{k}_{\|})-I(p,+\vec{k}_{\|})-I(s,-\vec{k}_{\|})+I(p,-\vec{k}_{\|})]/I_0. \quad (25c)$$

Because $A_{\mathrm{mag}}$ is the asymmetry due to incidence of unpolarized light, we have $A_{\mathrm{mag}}=\tilde{A}_{\mathrm{mag}}$. For the two other asymmetries, no similar relations hold.

The intensities in Fig. 9 for *s*- and *p*-polarized light are quite similar, in particular with photoelectron scattering included. This leads to rather small magnetization- and exchange-induced asymmetries but to a considerable polarization-induced asymmetry. Without photoelectron scattering, the spectra for *s*-polarized light appear to be nearly the same as for *p*-polarized light but scaled with a common factor. This becomes more transparent when considering $\tilde{A}_{\mathrm{pol}}$ which is nearly constant over the whole covered energy range. The exchange-related asymmetry shows the same shape as for circularly polarized light, which indicates that the ''magnetic'' information can be retrieved even for *s*- and *p*-polarized light.

### D. Photoelectron diffraction effects in off-normal emission

For thick films of bcc Fe(001) on Ag(001), Hillebrecht *et al.*[74] have performed experiments with normal light incidence (*s*-polarized light with electric-field vector along [010]) and off-normal emission within the $(0\bar{1}0)$ azimuth. The magnetization was either along [100] or $[\bar{1}00]$. In this setup, there is no double dichroism, but dichroism due to reversal of $\vec{M}$. For a fixed photon energy of 170 eV and binding energy of 51.8 eV, the authors of Ref. 74 obtained detection-angular scans and compared the experimental intensity differences with those of calculations which included photoelectron diffraction. The latter took into account only single-scattering events within a bulklike bcc Fe cluster. Further, the relative phases and amplitudes of the outgoing electron's partial waves had been fitted to obtain best agreement with experiment. A comparison of the experimental results with atomic calculations[75] suggests that effects due to scattering in the photoelectron state are of considerable strength.

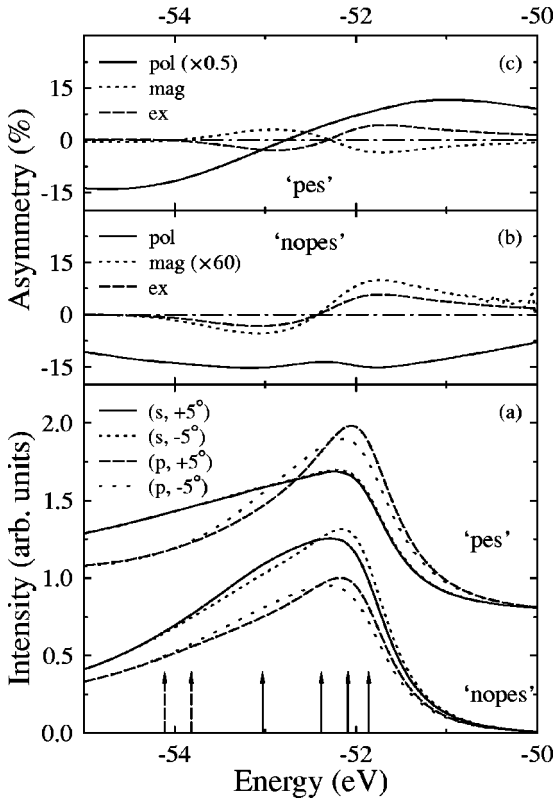


FIG. 9. Linear ''double'' dichroism from $3p$ levels of Fe(001) at 90 eV photon energy and 5° off-normal emission. (a) Intensities from calculations without (''nopes,'' bottom) and with (''pes,'' top) photoelectron scattering for two light polarizations $(s, p)$ and detection angles $(\pm 5°)$. Vertical arrows denote the $3p$ energy levels. (b) and (c) Asymmetries as defined in Eq. (25). In the ''nopes'' case (b), $A_{\mathrm{mag}}$ is scaled by a factor of 60, in the ''pes'' case (c) $A_{\mathrm{pol}}$ by a factor of 0.5. Line styles as indicated in panel (a).

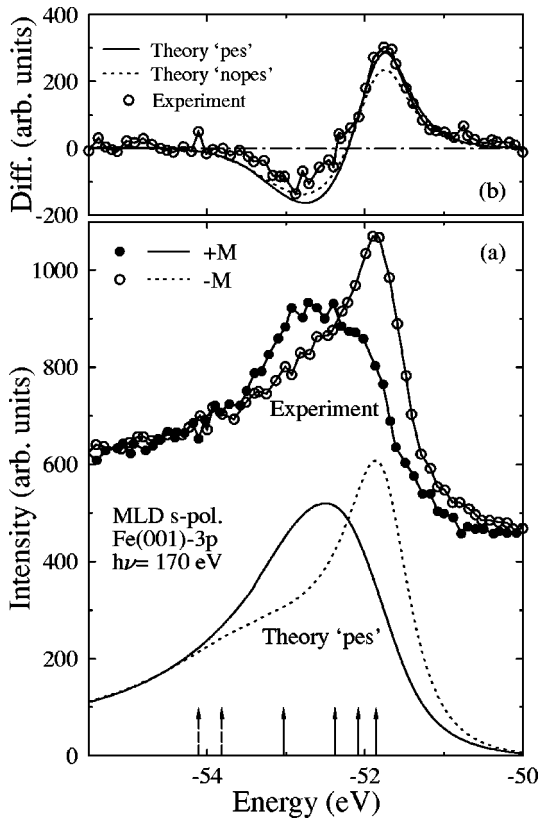


FIG. 10. Magnetic linear dichroism with $s$-polarized light from $3p$ levels of Fe(001) at $-45°$ polar angle of detection and 170 eV photon energy. (a) Theoretical with photoelectron scattering (lines, ''pes'') and experimental (circles) intensities. Vertical arrows indicate core-level positions obtained within the analytical model. (b) Differences of the intensities of panel (a). In addition, theoretically obtained differences without photoelectron scattering (''nopes'') are shown. Both panels use identical scales. Theoretical intensities are scaled in order to reproduce the experimental intensity at $-51.8$ eV.

In this section, we report on results obtained by our multiple-scattering approach for this system.

However, before turning to the $\vartheta_e$ scans, we address spectra for $\vartheta_e = -45°$ polar angle of detection (Fig. 10). The theoretical spectra agree very well with the experimental counterparts in shape. It should be noted that the theoretical spectra with photoelectron scattering have been scaled to obtain the experimental intensity at $-51.8$ eV. The spectra calculated without scattering in the photoelectron state (not shown here), however, are roughly reduced by a factor of 1.7 in intensity. Further, they exhibit minor changes in the spectral shape which become more apparent if the lifetime broadening is reduced.

The experimental spectra show an inelastic background which is not present in the difference spectra [Fig. 10(b)]. The theoretical counterparts (''pes'') agree very well in shape and size of the dichroism, in particular the maximum at $-51.8$ eV. The minimum at $-52.8$ eV is slightly overestimated in theory. Compared with atomic single-scattering calculations in Fig. 1 in Ref. 74 we observe a significant improvement in both shape and size of the dichroic signal. (Unfortunately, calculated intensities are not shown in Ref. 74 and, thus, cannot be compared with our results.) In particular, the small maximum at about $-54$ eV, which is due to initial states with highest binding energy, is not present in our work. This can be attributed to the lifetime broadening.

Switching off the photoelectron scattering reduces the dichroism slightly [Fig. 10(b)]. In other words, photoelectron scattering acts as an additional source of dichroism.[12] As for MCD in normal emission (Sec. IV B), there is a small shift to higher binding energies, which becomes larger if the lifetime broadening is reduced (not shown here).

Now we turn to the $\vartheta_e$ scans at fixed photon energy and binding energy. Due to the mirror symmetry of the setup, we have the symmetry relation $I(\pm\vec{M}, +\vartheta_e) = I(\mp\vec{M}, -\vartheta_e)$ which states that there is no dichroism in normal emission. Further, in atomic theories the dichroism vanishes for $\vartheta_e = \pm 90°$. In accordance with the ''general rule,'' there is a spin-orbit-induced ESP component along [100] for all other polar angles of detection and, thus, MLD. We have included the reduction of the first interlayer distance by a few percent,[76] a variation which effects the intensities only mildly.

At first, we address results obtained by the analytical atomic theory presented in Sec. III. Radial matrix elements and phase shifts have been taken from Ref. 75. From the energy positions of the initial states, it is clear that the state with $j = 3/2$ and $\mu = 3/2$ contributes most to the angular scan at 51.8 eV binding energy. Because we focus on the general

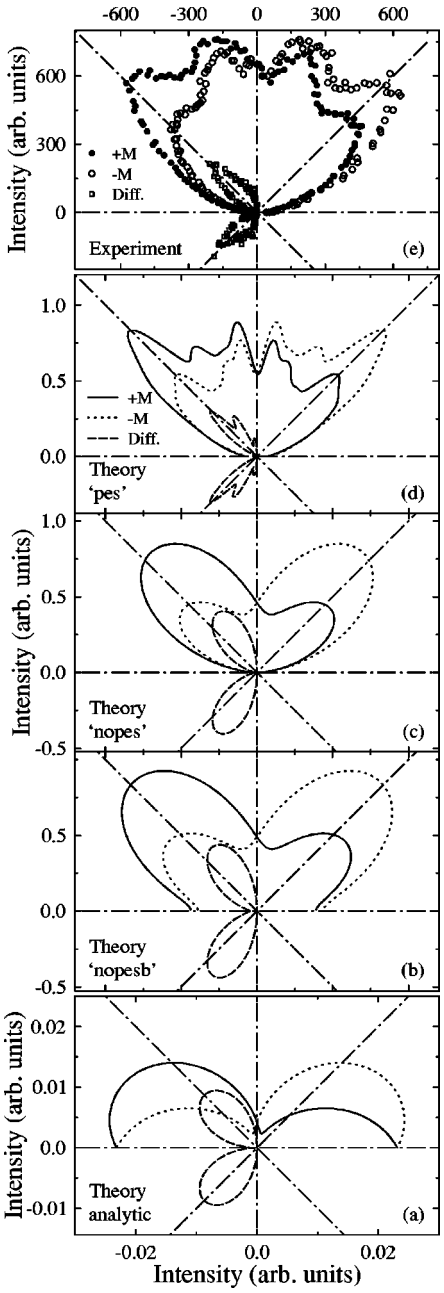


FIG. 11. Polar plots of magnetic linear dichroism from Fe(001) with *s*-polarized light with 170 eV photon energy at binding energy $-51.8$ eV and varying polar angle of detection. Normal emission refers to the *y* axis; dashed-dotted lines refer to 0°, ±45°, and 90° polar angle of detection, respectively. (a) Theoretical intensities for $+\vec{M}$ (solid line) and $-\vec{M}$ (dotted line) as well as their differences (MLD, dashed line) obtained within the analytical theory (Sec. III). (b) As in panel (a), but obtained by multiple-scattering theory without photoelectron scattering and surface barrier (''nopesb''). (c) As in panel (b), but with surface barrier (''nopes''). (d) As in panel (c), but with photoelectron scattering (''pes''). (e) Experimental intensities for $+\vec{M}$ (solid circles) and $-\vec{M}$ (open circles) as well as intensity differences (MLD) as squares. Reproduced from Ref. 74.

features, we show only this dominant contribution to the angular scan. In Fig. 11(a), the intensity distribution for the core state with $j=3/2$ and $\mu=3/2$ is shown. The angle of maximum intensity is 74°, and the intensity difference is proportional to $\sin 2\vartheta_e$, i.e., maximal at $\vartheta_e=\pm 45°$. Taking into account the asymmetry in the core-hole occupation[75] rotates the intensity distribution to a maximum angle of about ±32°; the angular dependence of the difference is not changed, however.

We also performed a weighted sum over the contributions of all initial states where the weights reflect both the energy position and the lifetime broadening of each individual state. First, we calculated the intensities of each initial state for $\vartheta_e=-45°$. Subsequently, these intensities were broadened by Lorentzians in order to come closer to experiment (Fig. 10). Finally, the individual parameters of the Lorentzians yield the weights. The result of this procedure is very close to that of the $(j=3/2,\mu=3/2)$ state alone: the shape of the angular distribution does not change significantly; the angle of maximum intensity is ±84°.

Second, we report on theoretical results obtained within our multiple-scattering theory with both photoelectron scattering and the surface barrier switched off [''nopesb,'' Fig. 11(b)]. Maximum intensity is obtained at ±44°. There is intensity at glancing detection angle—as in atomic theory—but also nonzero dichroism. This difference can be attributed to the emission from all atoms in the semi-infinite solid, as is present in one-step photoemission theory. Further, we observe additional intensity maxima at ±53° which are not present in atomic theory. The difference distribution shows nearly the same shape as that in Fig. 11(a), but with slightly rotated ''clubs'' with maximum angle ±34°. This shape distortion can be attributed to the occurrence of the maxima at ±53°.

In the next step, we switched on the surface barrier [''nopes,'' Fig. 11(c)]. The ''intensity clubs'' have become narrower, but most important is an intensity decay at higher detection angles: at $\vartheta_e=\pm 90°$ all beams—characterized by the surface-parallel lattice vector $\vec{g}$—are reflected by the surface barrier because $2E_{\mathrm{kin}}-(\vec{k}_{\parallel}+\vec{g})^2$ (in atomic units) becomes seminegative. Obviously, there is no emission for $\vartheta_e=\pm 90°$. The angles of maximum intensity are slightly shifted to ±41° and ±49°, respectively. The shape of the intensity distribution is affected considerably for large polar angles, but only mildly at small polar angles. Also the difference distribution is nearly the same as in Fig. 11(b).

Switching on photoelectron scattering [''pes,'' Fig. 11(d)] results in a drastic change of the intensity distribution. Instead of a rather smooth shape, the angular distribution shows now much more structure. In order to compare theory with experiment, we show theoretical results broadened with the experimental resolution (±3°). The experimental energy resolution (0.3 eV) has not been taken into account. Further, we neglect the energy and $\vec{k}_{\parallel}$ dependence of the surface-barrier shape. Thus, a perfect agreement between theory and experiment should not be expected.

Besides the main intensity maxima at ±46°, there are now minor maxima at ±30° and ±8° for $\pm\vec{M}$. In contrast to the ''nopes'' results [Fig. 11(c)], the maxima at ±46° and ±8° occur also for opposite polar angles but with different intensity. The position of the surface barrier affects in particular the ratio of the intensities of the maxima at ±8° and ±46°. The intensity difference has become narrower and rotated to maximum angle of ±46°. It shows further a sec-

ond, minor ''club'' at $\pm 30°$ which is due to the coincidence of the maximum in the $+\vec{M}$ with the minimum in the $-\vec{M}$ spectrum.

The experiment [Fig. 11(e)] shows two broad intensity maxima at around $\pm 45°$ and $\pm 13°$. Further, the intensity decays towards higher detection angles due to the surface barrier, as is evident from the comparison with Figs. 11(b) (''nopesb'') and 11(c) (''nopes''). Possibly due to uncertainties in the angular setup, there is a slight asymmetry of the data: in principle the mirror symmetry implies the relation $I(+\vec{M},\vartheta_e)=I(-\vec{M},-\vartheta_e)$ which is weakened in the experiment (cf. the distributions for $+\vec{M}$ and $-\vec{M}$ at small polar angles). Comparing with theory, the results shown in Fig. 11(d) agree reasonably well concerning the general shape of the intensity distribution.

Considering the difference distribution—which shows a maximum at about $\pm 45°$—we observe very good agreement with the theoretical results obtained with the full calculation [Fig. 11(d)] in both orientation of the clubs and the size of the dichroism. In a single-scattering calculation (cf. Fig. 2 in Ref. 74), the maximum intensity difference occurs at about $\pm 36°$.

In summary, we have analyzed in detail the effects of photoelectron scattering on MLD from Fe(001) $3p$ using several approximations to the full calculation. The manifestation of the solid shows a pronounced effect on the angular distribution which shows that multiple scattering has to be taken into account, in particular in off-normal emission.

### E. Magnetic linear dichroism from 3*p* levels of Ni(110)

Recently, Sacchi *et al.*[77] reported on experiments and corresponding atomic multiplet calculations of MLD from $3p$ levels of Ni(110). These calculations were able to reproduce the experimental spectral shapes very well but overestimated the dichroism by a factor of about 10. The reason for this was unclear. We performed corresponding calculations within the multiple-scattering scheme with and without photoelectron scattering in order to investigate whether photoelectron scattering can be made responsible for the above observation. A main point in the work of Sacchi *et al.* was the satellite structures at 6 eV and 14 eV below the main line. We cannot address this important feature because our work is performed within the independent-particle picture. The main line, however, should be reproducible. For details of the experimental setup we refer to the paper of Sacchi *et al.* In our calculations, the surface relaxation was taken into account.[78]

Fitting the analytically obtained energy levels to those obtained by the Dirac equation without scaling of SOC and exchange we obtain $\lambda=1.47$ eV and $\zeta=0.78$ eV ($x=0.65$); thus we are dealing with well separated $3p_{1/2}$ and $3p_{3/2}$ levels. In order to reproduce the experiment, we have scaled SOC and exchange by factors of 0.95 and 0.37, respectively. Thus, SOC is strong compared to exchange ($x=0.83$ and $\zeta/\lambda=0.20$); cf. the vertical arrows in Fig. 12(a).

In addition to the multiple-scattering calculations, we show in Fig. 12(a) results obtained within the analytical model for the free atom with parameters taken from Ref. 63. The intensities were broadened with Lorentzians with widths of 1.15 eV and 1.00 eV for the $3p_{1/2}$ and $3p_{3/2}$ states, respectively. This leads—in contrast to energy-dependent lifetimes in the multiple-scattering calculations (with parameters $a=0.2$, $E_0=-65.8$ eV, $b=1.0$ for the core hole, $a=4.0$, $b=0.0$ for the photoelectron)—to an intensity increase (decrease) at higher (lower) energies compared to the experimental data. The main peak in the spectrum at 105.8 eV is due to $3p_{3/2}$ levels, the shoulder at 103.9 eV due to $3p_{1/2}$ levels. Considering the intensity differences, we find a strong overestimation of the MLD [Fig. 12(b)]. In particular, the maximum at 105.3 eV is by far too high. However, the shape of the ''minus'' feature at 106.4 eV is well reproduced. In contrast to the experiment, a second pronounced minimum occurs at 103.3 eV. The asymmetry at 106.8 eV is $-4.8\%$, which overestimates the experimental value of $-1.25\%$ by a factor of about 3.

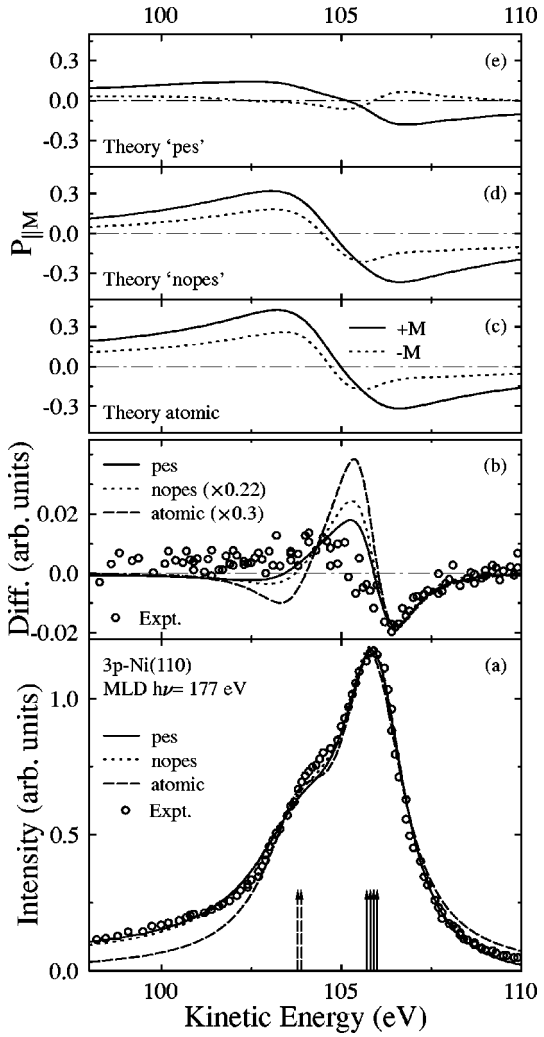


FIG. 12. Magnetic linear dichroism from $3p$ levels of Ni(110). (a) Theoretical (solid, dotted, and dashed lines) and experimental (circles, reproduced from Ref. 77) intensities averaged over both magnetization directions. ''pes'' (solid lines) refer to multiple-scattering calculations with photoelectron scattering taken into account, ''nopes'' (dotted lines) to those without photoelectron scattering. ''atomic'' (dashed lines) are results obtained within the analytical model for the atom. Vertical arrows denote core-level energies. (b) Differences of the intensities shown in panel (a). Line styles as is indicated in panel (a). (c), (d), and (e) Theoretical spin polarization parallel to the magnetization for $+\vec{M}$ (solid) and $-\vec{M}$ (dotted) for the three calculations as indicated.

In the multiple-scattering calculations, we observe good agreement to experiment in the spectral shape of the intensities averaged over the magnetization directions, regardless of whether we take into account photoelectron scattering (''pes'') or not (''nopes''). This finding agrees nicely with that for MCD from Fe(001) in normal emission. Small deviations occur at the shoulder around 103.9 eV kinetic energy which also occur in the multiplet calculations in Ref. 77. Considering the intensity differences [Fig. 12(b)], both theoretical calculations reproduce the experimental data well, in particular the minimum at around 105.8 eV. Turning to the asymmetry, the calculation with photoelectron scattering shows a minimum of $-1.3\%$ at 106.8 eV which agrees very well with that obtained experimentally ($-1.25\%$). Neglecting the photoelectron scattering, however, leads to a minimum asymmetry of $-5.5\%$ and a slight narrowing of the maximum. We consider the above results as evidence that the disagreement in size of the MLDAD in Ref. 77 can be explained by scattering of the outgoing electron.

At last, we address briefly the effect of photoelectron scattering on the spin polarization of the outgoing electron; cf. Figs. 12(c)–12(e)]. For the current setup, the ESP of each core-hole state is complete ($\vec{P} \| \vec{M}$ and $|\vec{P}| = 1$). The general trend—positive ESP for the $3p_{1/2}$ states, negative for the $3p_{3/2}$ states—is clearly visible in the calculations which do not take into account photoelectron scattering [Figs. 12(c) and 12(d)]. In particular, the results in the cases ''nopes'' and ''atomic'' agree very well. A strong reduction of the absolute value of the ESP is obtained in the ''pes'' case [Fig. 12(e)]. Even a sign change occurs (cf. the dotted line around 105.9 eV). In our opinion, these findings suggest the need of more spin-resolved dichroic experiments in order to investigate this manifestation of scattering in MD.

## V. CONCLUSIONS

For prototypical systems—$3p$ levels of Fe and Ni at (001) and (110) surfaces, respectively—magnetic circular and linear dichroism in angle-resolved photoemission have been investigated within the relativistic one-step model of photoemission in the framework of multiple-scattering theory (layer KKR). Scaling the strength of both spin-orbit coupling and exchange allows for a successful description of the experiments. Multiple scattering within the photoelectron state has a profound effect on intensities, dichroism, and spin polarization, in particular in off-normal emission. In normal emission, the photocurrent is affected only mildly.

Photoemission from ferromagnets in a chiral setup leads to so-called ''double'' dichroism, i.e., a combination of circular dichroism in angular distribution with magnetic circular dichroism. Using appropriately defined asymmetries, we showed how to separate both effects.

A simple analytical model of photoemission from atoms is found to reproduce energy positions and compositions of core-hole states which have been obtained by fully relativistic calculations. Even dichroic photoemission and spin polarization compare well with numerical one-step photoemission results and experiments in normal emission. In off-normal electron detection—when photoelectron scattering becomes more important—strong deviations occur.

## ACKNOWLEDGMENTS

We appreciate fruitful discussions with T. Scheunemann (Duisburg). This work was performed within the Training and Mobility of Researchers (TMR) Network ''Interface Magnetism.'' We also thank the Swedish Natural Science Research Council (NFR) and the Swedish Materials Consortium No. 9 financed by SSF for valuable support.

[1] L. Baumgarten, C. M. Schneider, H. Petersen, F. Schäfers, and J. Kirschner, Phys. Rev. Lett. **65**, 492 (1990).
[2] F. U. Hillebrecht, C. Roth, H. B. Rose, W. G. Park, E. Kisker, and N. A. Cherepkov, Phys. Rev. B **53**, 12 182 (1996).
[3] J. G. Menchero, Phys. Rev. B **57**, 993 (1998).
[4] G. van der Laan, J. Magn. Magn. Mater. **148**, 53 (1995).
[5] G. van der Laan, J. Electron Spectrosc. Relat. Phenom. **86**, 41 (1997).
[6] G. van der Laan, J. Phys.: Condens. Matter **9**, L259 (1997).
[7] G. van der Laan, Phys. Rev. B **57**, 5250 (1998).
[8] J. G. Menchero, Phys. Rev. B **57**, 1001 (1998).
[9] A. Fanelsa, R. Schellenberg, F. U. Hillebrecht, E. Kisker, J. G. Menchero, A. P. Kaduwela, C. S. Fadley, and M. A. Van Hove, Phys. Rev. B **54**, 17 962 (1996).
[10] J. G. Menchero, C. S. Fadley, G. Panaccione, F. Sirotti, and G. Rossi, Solid State Commun. **103**, 197 (1997).
[11] J. G. Menchero, Phys. Rev. B **55**, 5505 (1997).
[12] R. Schellenberg, E. Kisker, A. Fanelsa, F. U. Hillebrecht, J. G. Menchero, A. P. Kaduwela, C. S. Fadley, and M. A. V. Hove, Phys. Rev. B **57**, 14 310 (1998).
[13] H. Ebert, L. Baumgarten, C. M. Schneider, and J. Kirschner, Phys. Rev. B **44**, 4406 (1991).
[14] H. Ebert and G.-Y. Guo, J. Magn. Magn. Mater. **148**, 178 (1995).
[15] E. Tamura, G. D. Waddill, J. G. Tobin, and P. A. Sterne, Phys. Rev. Lett. **73**, 1533 (1994).
[16] D. Venus, J. Magn. Magn. Mater. **170**, 29 (1997).
[17] D. Venus, W. Kuch, M.-T. Lin, C. M. Schneider, H. Ebert, and J. Kirschner, Phys. Rev. B **55**, 2594 (1997).
[18] D. Venus, Phys. Rev. B **56**, 2661 (1997).
[19] R. Feder and J. Henk, in *Spin-Orbit Influenced Spectroscopies of Magnetic Solids*, Vol. 466 of *Lecture Notes in Physics*, edited by H. Ebert and G. Schütz (Springer, Berlin, 1996), p. 85.
[20] T. Scheunemann, S. Halilov, J. Henk, and R. Feder, Solid State Commun. **91**, 487 (1994).
[21] J. Henk, S. Halilov, T. Scheunemann, and R. Feder, Phys. Rev. B **50**, 8130 (1994).
[22] J. Henk, T. Scheunemann, S. Halilov, and R. Feder, J. Phys.: Condens. Matter **8**, 47 (1996).
[23] J. Henk and R. Feder, Phys. Rev. B **55**, 11 476 (1997).
[24] J. Henk and B. Johansson, J. Electron Spectrosc. Relat. Phenom. **94**, 259 (1998).
[25] A. Fanelsa, E. Kisker, J. Henk, and R. Feder, Phys. Rev. B **54**, 2922 (1996).
[26] W. Kuch, A. Dittschar, K. Meinel, M. Zharnikov, C. Schneider, J. Kirschner, J. Henk, and R. Feder, Phys. Rev. B **53**, 11 621 (1996).
[27] W. Kuch, M. Zharnikov, A. Dittschar, K. Meinel, C. Schneider, J. Kirschner, J. Henk, and R. Feder, J. Appl. Phys. **79**, 6426 (1996).

[28] A. Rampe, G. Güntherodt, D. Hartmann, J. Henk, T. Scheunemann, and R. Feder, Phys. Rev. B **57**, 14 370 (1998).
[29] M. Wöhlecke and G. Borstel, in *Optical Orientation*, edited by F. Meier and B. P. Zakharchenya (North-Holland, Amsterdam, 1984).
[30] E. Tamura, W. Piepke, and R. Feder, Phys. Rev. Lett. **59**, 934 (1987).
[31] E. Tamura and R. Feder, Europhys. Lett. **16**, 695 (1991).
[32] J. Henk and R. Feder, Europhys. Lett. **28**, 609 (1994).
[33] C. Westphal, F. Fegal, J. Bansmann, M. Getzlaff, G. Schönhense, J. A. Stephens, and V. McKay, Phys. Rev. B **50**, 17 534 (1994).
[34] G. Fecher, Europhys. Lett. **29**, 605 (1995).
[35] We use the terms ''initial'' and ''final'' states as synonyms for core-level and photoelectron states, respectively, in an independent-particle picture. In many-particle language, these terms would describe the state of the many-electron system before and after excitation.
[36] *Polarized Electrons in Surface Physics*, *Advanced Series in Surface Science*, edited by R. Feder (World Scientific, Singapore, 1985).
[37] *Electron Scattering Theory of Ordered and Disordered Matter*, edited by P. Weinberger (Clarendon Press, Oxford, 1990).
[38] O. K. Andersen, Phys. Rev. B **12**, 3060 (1975).
[39] H. L. Skriver and N. M. Rosengaard, Phys. Rev. B **43**, 9538 (1991).
[40] M. Aldén, H. L. Skriver, and B. Johansson, Phys. Rev. Lett. **71**, 2449 (1993).
[41] M. Aldén, I. A. Abrikosov, B. Johansson, N. M. Rosengaard, and H. L. Skriver, Phys. Rev. B **50**, 5131 (1994).
[42] M. Aldén, H. L. Skriver, and B. Johansson, Phys. Rev. B **50**, 12 118 (1994).
[43] J. Pendry, Surf. Sci. **57**, 679 (1976).
[44] J. Hopkinson, J. Pendry, and D. Titterington, Comput. Phys. Commun. **19**, 69 (1980).
[45] J. Braun, Rep. Prog. Phys. **59**, 1267 (1996).
[46] PEOVER is the name of a photoemission computer program which is based on the theory of Pendry (Ref. 43) and introduced in Ref. 44.
[47] E. Tamura, Phys. Rev. B **45**, 3271 (1992).
[48] E. Tamura, in *Applications of Multiple Scattering Theory to Materials Science*, edited by W. H. Butler, P. H. Dederichs, A. Gonis, and R. L. Weaver (Materials Research Society, Pittsburgh, 1992), p. 347.
[49] P. Feibelman and D. Eastman, Phys. Rev. B **10**, 4932 (1974).
[50] H. Wu, C. Y. Ng, T. P. Chu, and S. Y. Tong, Phys. Rev. B **57**, 15 476 (1998).
[51] Y. Chen, F. J. G. de Abajo, A. Chassé, R. X. Ynzunza, A. P. Kaduwela, M. A. V. Hove, and C. S. Fadley, Phys. Rev. B **58**, 13 121 (1998).
[52] G. Y. Guo, Phys. Rev. B **57**, 10 295 (1998).
[53] J. F. Hart and J. L. Beeby, Surf. Sci. **410**, L757 (1998).
[54] H. Ebert, J. Phys.: Condens. Matter **1**, 9111 (1989).
[55] E. Tamura (private communication).
[56] H. Ebert, H. Freyer, A. Vernes, and G. Y. Guo, Phys. Rev. B **53**, 7721 (1996).
[57] H. Ebert, H. Freyer, and M. Deng, Phys. Rev. B **56**, 9454 (1997).
[58] D. D. Koelling and B. N. Harmon, J. Phys. C **10**, 3107 (1977).
[59] H. Gollisch and L. Fritsche, Phys. Status Solidi B **86**, 156 (1978).
[60] T. Takeda, J. Phys. F **9**, 815 (1979).
[61] R. Feder, in *Polarized Electrons in Surface Physics*, *Advanced Series in Surface Science*, edited by R. Feder (World Scientific, Singapore, 1985), Chap. 4, p. 125.
[62] G. van der Laan, Phys. Rev. B **51**, 240 (1995).
[63] S. Goldberg, C. Fadley, and S. Kono, J. Electron Spectrosc. Relat. Phenom. **21**, 285 (1981).
[64] C. Roth, J. Magn. Magn. Mater. **148**, 58 (1995).
[65] E. M. Rose, *Relativistic Electron Theory* (Wiley, New York, 1961).
[66] J. G. Tobin, K. W. Goodman, F. O. Schumann, R. F. Willis, J. B. Kortright, J. D. Denliger, E. Rotenberg, A. Warwick, and N. V. Smith, Surf. Sci. **395**, L227 (1998).
[67] A. Lindner, *Drehimpulse in der Quantenmechanik* (B. G. Teubner, Stuttgart, 1984).
[68] A computer program based on the theory of Sec. III can be obtained from the authors (electronic address: jurgen@fysik.uu.se).
[69] J. Kessler, *Polarized Electrons*, Vol. 1 of *Springer Series on Atoms and Plasmas*, 2nd ed. (Springer, Berlin, 1985).
[70] *Photoemission in Solids I*, Vol. 26 of *Topics in Applied Physics*, edited by M. Cardona and L. Ley (Springer, Berlin, 1978).
[71] F. U. Hillebrecht, C. Roth, H. B. Rose, E. Kisker, M. Finazzi, and L. Braicovich, Phys. Rev. B **51**, 9333 (1995).
[72] F. Sirotti and G. Rossi, Phys. Rev. B **49**, 15 682 (1994).
[73] G. Rossi, F. Sirotti, N. A. Cherepkov, and F. C. F. G. Panaccione, Solid State Commun. **90**, 557 (1994).
[74] F. U. Hillebrecht, H. B. Rose, T. Kinoshita, Y. U. Idzerda, G. van der Laan, R. Denecke, and L. Ley, Phys. Rev. Lett. **75**, 2883 (1995).
[75] G. van der Laan, Phys. Rev. B **55**, 3656 (1997).
[76] K. O. Legg, F. Jona, D. W. Jepsen, and P. M. Marcus, J. Phys. C **10**, 937 (1977).
[77] M. Sacchi, G. Panaccione, J. Vogel, A. Mirone, and G. van der Laan, Phys. Rev. B **58**, 3750 (1998).
[78] Y. Gauthier, R. Baudoing, Y. Joly, C. Gaubert, and J. Rundgren, J. Phys. C **17**, 4547 (1984).